The Astrophysical Journal, 729:144 (8pp), 2011 March 10 doi:10.1088/0004-637X/729/2/144

APODIZED PUPIL LYOT CORONAGRAPHS FOR ARBITRARY APERTURES. III. QUASI-ACHROMATIC SOLUTIONS

Rémi Soummer[1], Anand Sivaramakrishnan[1,5,6,7], Laurent Pueyo[1,2], Bruce Macintosh[3], and Ben R. Oppenheimer[4]
[1] Space Telescope Science Institute, 3700 San Martin Drive, Baltimore, MD 21218, USA; soummer@stsci.edu, anand@stsci.edu
[2] Department of Physics & Astronomy, Johns Hopkins University, 366 Bloomberg Center, 3400 N. Charles St., Baltimore, MD 21218, USA; lap@pha.jhu.edu
[3] Lawrence Livermore National Laboratory, 7000 East Avenue, Livermore, CA 94550, USA; macintosh1@llnl.gov
[4] Department of Astrophysics, American Museum of Natural History, 79th Street Central Park West, New York, NY 10024, USA; bro@amnh.org
Received 2010 July 19; accepted 2011 January 12; published 2011 February 22

ABSTRACT

Direct imaging and spectroscopy of young giant planets from the ground requires broadband starlight suppression with coronagraphy. It is important to minimize the coronagraph chromatic sensitivity to help remove residual speckles through post-processing of images at multiple wavelengths. The coronagraph must also be able to mitigate the effects of ground-based telescopes with central obstruction. We present new properties of the Apodized Pupil Lyot Coronagraph (APLC) that enable quasi-achromatic starlight suppression over a broad bandpass (20%) and with central obstructions. We discuss the existence of these quasi-achromatic solutions using the properties of the generalized prolate spheroidal functions, which are used to define the apodizer profile. We discuss a broadband optimization method and illustrate its parameter space in terms of inner working angle and contrast. These new APLC solutions are implemented in the Gemini Planet Imager (GPI), a new facility instrument to detect and characterize young giant planets and disks, which will be commissioned in 2011. The coronagraph design delivers a contrast better than 10^{-7} beyond a separation of 0.2 arcsec in the presence of Gemini's central obstruction over a 20% bandpass. The science camera is an integral field spectrograph observing in one of the *Y*, *J*, or *H*, or in about two-thirds of the *K* bandpass, at a single time. Similar solutions have also been used for the Palomar 1640 coronagraphic integral field spectrograph.

Key words: infrared: planetary systems – instrumentation: high angular resolution – techniques: high angular resolution

Online-only material: color figures

1. INTRODUCTION

Among the large number of currently known exoplanets (Schneider 2010), few have been detected with direct imaging (Marois et al. 2008a; Kalas et al. 2008; Lagrange et al. 2009), let alone characterized with spectroscopy (Janson et al. 2010; L. Pueyo et al. 2011, in preparation). In the near future, direct imaging detections will increase dramatically with new instruments becoming available on large ground-based telescopes, including the Gemini Planet Imager (GPI; Macintosh et al. 2008), SPHERE (Beuzit et al. 2008), Palomar Project 1640 (Hinkley et al. 2008; Hinkley et al. 2010b), and Subaru HiCIAO (Hodapp et al. 2008). These instruments will typically be able to obtain images and low-resolution spectra of relatively young giant planets (few hundred million years old) and brown dwarfs around nearby stars. According to theoretical models, contrast ratios of about 10^{-7} are expected for 100 Myr old, Jupiter-mass objects in the near-infrared *J*, *H*, and *K* bandpasses (Baraffe et al. 2003; Burrows et al. 2004; Marley et al. 2007).

One significant difficulty for direct imaging, once the wavefront error is well controlled, is the presence of diffracted starlight (Oppenheimer & Hinkley 2009). Coronagraphy is one of the main techniques used to achieve starlight suppression for high-contrast imaging. Because the planets of interest are located at very small separations (few tenth of a second of arc), coronagraphs must be able to achieve starlight suppression at small inner working angles (IWAs). Moreover, this must be obtained in the presence of telescope central obstruction and over a broad band (typically 20%). The classical Lyot Coronagraph (Lyot 1939; Sivaramakrishnan et al. 2001) does not provide sufficient starlight suppression to enable the detection of extrasolar planets, and several more advanced techniques have been proposed in the past few years (Roddier & Roddier 1997; Rouan et al. 2000; Baudoz et al. 2000; Aime et al. 2002; Kuchner & Traub 2002; Soummer et al. 2003b; Kasdin et al. 2003; Guyon et al. 2005; Mawet et al. 2005; Foo et al. 2005; Serabyn et al. 2010; L. Pueyo et al. 2011, in preparation; Crepp et al. 2011). Some of these techniques have already been developed in the laboratory and tested on the sky.

In this paper, we consider the Apodized Pupil Lyot Coronagraph (APLC) developed by Aime et al. (2002) and Soummer et al. (2003a) for rectangular and circular aperture geometries and generalized by Soummer (2005) and Soummer et al. (2009a) for telescopes with arbitrarily shaped apertures. We study the chromatic effects in these coronagraphs and derive quasi-achromatic solutions to enable starlight suppression over the typical bandpasses considered for ground-based observations limited by atmospheric windows in the near-infrared. The APLC was selected for a number of advantages for GPI and Palomar 1640. These include the compatibility with telescope central obstruction, the possibility of high contrast in broadband ($\simeq 10^7$), good IWA ($\simeq 4\lambda/\mathcal{D}$), and relatively high coronagraphic throughput for the off-axis target ($\simeq$50%). The APLC involves a hard-edged focal plane mask that can be manufactured with excellent quality using a hole in a mirror (Oppenheimer et al. 2004; Soummer et al. 2009b; Sivaramakrishnan et al. 2010).

[5] Department of Astrophysics, American Museum of Natural History, 79th St. Central Park West, New York, NY 10024, USA.
[6] NSF Center for Adaptive Optics.
[7] Physics and Astronomy, SUNY Stony Brook, Stony Brook, NY 11794.

The starlight passing through the hole enables an elegant implementation of a second-stage wavefront sensing system with a Mach–Zendher interferometer (Wallace et al. 2008; Sivaramakrishnan et al. 2008), which does not introduce any non-common path errors up to the focal plane mask.

The first two difficulties to overcome are the presence of a central obstruction and the necessity of broadband observations to enable spectroscopy. Generalized prolate spheroidal apodizations for a centrally obscured aperture provide an excellent way of mitigating the geometric constraints. In principle, secondary mirror support structures can also be included in the optimization of the apodizer (Soummer et al. 2009a). However, in the case of very thin structures such as for the Gemini telescope (1 cm) this would lead to a non-rotationally symmetric apodizer with additional system-level complexities that are not worth the potential gain, especially since the effect of these features can be mitigated in the Lyot plane (Sivaramakrishnan & Lloyd 2005). Other techniques such as the phase-induced amplitude apodization (Guyon et al. 2005; Pluzhnik et al. 2006; Martinache et al. 2006) can be used to mitigate central obstruction and spiders, but add complexity with more optics. This solution was used for the Subaru telescope geometry with large support structures (Martinache & Guyon 2009). GPI and Project 1640 both use multi-wavelength images from an integral field spectrograph to help distinguish true companions from speckle artifacts (Marois et al. 2000; Sparks & Ford 2002) and to provide the companion spectrum. Post-processing reference subtraction algorithms (Lafrenière et al. 2007) are facilitated when the planet spectrum is significantly different from the residual coronagraphic response. A chromatically flat coronagraphic response is generally considered the most favorable case (Krist et al. 2008).

In Section 2, we recall the principle of APLCs and focus on their chromatic properties and limitations. In Section 3, we develop a numerical optimization for broadband observations and show that quasi-achromatic solutions can be obtained, and we discuss the existence of these solutions using the properties of the generalized prolate functions. The study assumes gray transmission apodizers, which can be manufactured using halftone (microdots) or star-shaped technologies (Martinez et al. 2009a, 2009b; Sivaramakrishnan et al. 2009; Soummer et al. 2009b; Cady et al. 2009).

2. CHROMATIC PROPERTIES OF APODIZED PUPIL LYOT CORONAGRAPHS

2.1. Impact of Chromaticity on Contrast Performance

Ground-based AO coronagraphs will almost certainly be limited by residual point-spread function (PSF) speckles caused by atmospheric and instrumental phase and amplitude errors. (See Marois et al. 2008b for a discussion of many classes of error.) To overcome these speckles, simultaneous images at multiple wavelengths will be obtained using either an integral field unit, or a dual- or a multi-band camera. This spectral information can be used to distinguish speckle artifacts from true companions using either the radial scaling of speckle position with wavelength or strong spectral features in the planetary companion. Images at multiple wavelengths, scaled radially to align the speckles, can be subtracted from each other (Marois et al. 2006) or simple functions are fit to the intensity in each pixel as a function of wavelength (Sparks & Ford 2002; L. Pueyo et al. 2011, in preparation). For this process to significantly attenuate noise, both the speckles themselves and the coronagraph must be achromatic over a large enough range of wavelengths $\Delta\lambda$ so that the speckles have either moved by a significant fraction of the diffraction limit ($\Delta\lambda/\lambda = \theta/(\lambda/\mathcal{D})$) or a range comparable to the width of typical molecular absorption features, $\Delta\lambda = 0.1\,\mu$m.

The signal-to-noise ratio for planet detection is determined by the combination of the coronagraphic response to a perfect wave with the residual intensity halos created by the optical aberrations. Aime & Soummer (2004) and Soummer et al. (2007a) have shown that the speckle noise from "pinned" speckles (Bloemhof et al. 2001; Sivaramakrishnan et al. 2002; Bloemhof 2003; Perrin et al. 2003) can be reduced with a coronagraph. The variance of the speckles and photon noise in a coronagraphic image is given by

$$\sigma^2 = 2I_c I_s + I_s^2 + I_c + I_s, \quad (1)$$

where I_c is the final focal plane intensity through the coronagraph in the absence of random aberrations (static aberrations are included in this term) and I_s corresponds to the intensity halo produced by optical aberrations (Aime & Soummer 2004). The last two terms $I_c + I_s$ correspond to the photon noise and are scaled appropriately for an exposure time corresponding to the speckle lifetime (Soummer et al. 2007a). The speckle statistics was confirmed by Fitzgerald & Graham (2006) using adaptive optics images. The coronagraph is particularly important to this process. For given residual adaptive optics aberrations, the variance is minimum for $I_c = 0$, i.e., a perfect coronagraph. Since pinned speckles have a variance proportional to both the intensity of the speckles and the residual intensity of the coronagraph (Equation (1)), a sharp variation in coronagraph contrast with wavelength (as in the smaller diameter masks in Figure 4) will produce an equally sharp variation in the intensity of speckles with wavelength that is not easily fit by linear or low-order functions. Hence, for full spectral suppression of residual speckles, it is important that the variation in coronagraph intensity over the operational wavelength range be comparable to or less than the final design contrast of the system. This was confirmed independently using end-to-end simulations for GPI (Marois et al. 2008b).

2.2. Principle and Chromatic Properties

We briefly recall here the principle of an APLC with emphasis on its chromatic behavior. The coronagraph involves three optical masks (apodizer, focal plane mask, and Lyot stop), in four successive planes illustrated in Soummer et al. (2009a) (Figure 1). In the perfect monochromatic case, an optimal set of masks exists and is determined by the solution of an eigenvalue problem (Aime et al. 2002; Soummer et al. 2003a; Soummer 2005; Soummer et al. 2009a). In this paper, we study the case of circular geometry with central obstruction, where the apodization function (eigenfunction) is given by a generalized prolate spheroidal function (Slepian 1964; Soummer 2005) and the FPM diameter is associated with the eigenvalue. This result also holds for more complex aperture shapes, such as an Extremely Large Telescope (ELT) segmented design (Soummer et al. 2009a).

We follow the formalism of Aime et al. (2002) and Soummer et al. (2003a), and restrict the problem to the case of a circular focal plane mask of physical diameter d, whose transmission is $1 - M(\mathbf{r})$, with $M(r) = \Pi(r/d)$, $r = |\mathbf{r}|$, and where $\Pi(r)$ denotes the top-hat radial function. It is convenient to express the FPM diameter in resolution element units and we introduce

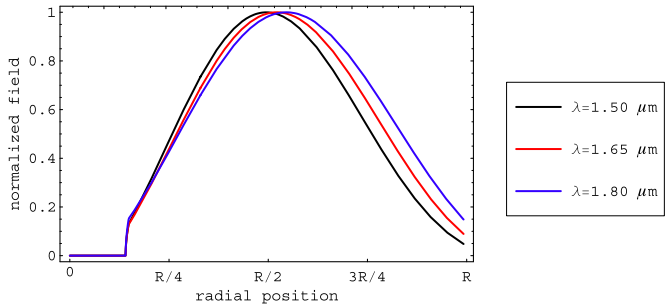

Figure 1. Radial profiles of the achromatic apodization for three wavelengths across the *H* band for the Gemini telescope geometry. The apodizer has a "bagel-shaped" transmission (note that the plot represents a radial profile from the center to the edge of the pupil of radius *R*). A different eigenvalue problem exists for each wavelength and the theoretical optimal apodizer corresponds to a different prolate function (Aime 2005).

(A color version of this figure is available in the online journal.)

the notations

$$d = \alpha_1 \frac{\lambda_1 f}{\mathcal{D}} = a_1 \lambda_1 f, \tag{2}$$

where $\mathcal{D}$ is the telescope diameter, f is the focal length, and α_1 corresponds to the diameter of the FPM expressed in units of resolution element, and $a_1 = \alpha_1/\mathcal{D}$ is a notation introduced by Soummer et al. (2003a) for clarity.

It is essential to note that we define the FPM diameter at a reference wavelength λ_1, as indicated by the subscript in α_1 and a_1. The value of this wavelength is critical to the optimization approach described in this paper. Using the scaling properties of Fourier transforms (FTs), the two-dimensional FT of the mask function is $\widehat{M}(\mathbf{u}) = d^2\,\widehat{\Pi}(d\,\mathbf{u})$, where $\mathbf{u} = (\eta, \xi)$ is the spatial frequency. Using the equivalent mask parameter $a = a_1\lambda_1/\lambda$, and the fact that the two-dimensional FT of the circular top-hat function $M(r)$ is also a radial function $\widehat{\Pi}(u) = (\pi/4)(2J_1(\pi u))/(\pi u)$, we obtain

$$\Psi_C(\mathbf{r}) = \Psi_A(\mathbf{r}) - \Psi_A(\mathbf{r}) * \frac{a J_1(\pi a r)}{2r}. \tag{3}$$

Note that $*$ is a two-dimensional convolution product (see, for example, Equation (3) in Aime et al. (2002) with the $1/(\lambda f)^2$ term from the change of variables in the two-dimensional convolution product). Also, note that $\Psi_A(\mathbf{r})$ and $\Psi_C(\mathbf{r})$ are not necessarily radial functions, although $a J_1(\pi a\, r)/(2\, r)$ is. We can see in Equation (3) that the propagation wavelength λ solely affects the equivalent mask size a. In other words, a change of propagation wavelength λ is formally equivalent to a change of mask size. This is simply because for a given physical FPM size (a hard-edged mask), each wavelength corresponds to a different mask size in resolution element units ($\lambda/\mathcal{D}$). This has a direct consequence for numerical simulations: monochromatic propagation codes can readily be adapted to polychromatic simulations by scaling the effective mask size by λ_1/λ.

The final coronagraphic field is obtained from the field in the Lyot plane, after application of the Lyot stop $L(\mathbf{r})$. In the perfect case, the Lyot stop is simply identical to the pupil and no undersizing is required. In practice, some amount of undersizing is required for alignment tolerancing reasons.

2.3. Broadband Performance, Achromatic APLCs

Aime (2005) showed that the equivalent mask size a implies a different eigenvalue for each wavelength, and therefore that a different eigenfunction (apodizer) can be calculated for each wavelength (Equation (3)). This is illustrated in Figure 1 in the case of an apodizer with central obstruction, where the apodizer corresponds to a different prolate function for each wavelength. This effect could be achieved for example using interferometry (Carlotti et al. 2008) or approximated using a colored absorbing glass (Soummer et al. 2006). In the case of a telescope with central obstruction, these ideal solutions would be very challenging to reproduce in practice because the position of the maximum transmission depends on the wavelength. In this paper, we explore the parameter space for the APLC and outline a regime where the solution is quasi-achromatic for slightly larger FPM sizes. If we assume a gray apodizer, i.e., same apodization function for every wavelength, and a physical hard-edged FPM such as a hole in a mirror, the prolate apodizer solution is defined at a single wavelength and the performance degrades when the wavelength changes (Equation (3)).

3. BROADBAND OPTIMIZATION OF APLCs

3.1. Optimization Criteria and Parameter Space Exploration

As detailed above, APLCs are defined by analytical solutions to an eigenvalue problem in the monochromatic case. In this section, we study the numerical optimization of the APLC in broad band and explore the parameter space of the possible solutions assuming a gray apodizer (achromatic apodization profile) and a given physical FPM. Therefore, one wavelength must be chosen to define the eigenvalue problem and generate the apodizer (eigenfunction).

Several criteria can be considered for the optimization of APLCs (Martinez et al. 2007, 2008; Soummer et al. 2009a). The simplest criterion is the integrated residual intensity, which can be calculated readily in the Lyot plane and provides some interesting insight into the coronagraphic efficiency. However, this criterion is not sufficient for high-contrast imaging because it does not provide any indication about the distribution of the light in the final image plane. In Soummer (2005), we used the encircled energy within the mask area for the optimization criterion, with a simple optimization approach. In this paper, we consider the average contrast inside the dark zone controlled by the deformable mirror and outside the IWA. In the case of GPI, this corresponds to a square of side $\mathcal{N} = 44\lambda/\mathcal{D}$, corresponding to the 44 actuators across the pupil diameter $\mathcal{D}$. The IWA corresponds to the minimum distance at which the transmission of an off-axis companion is significantly high. For the optimization of the APLC parameters, we consider the IWA to be equal to the mask radius augmented by two resolution elements. The actual IWA in terms of detection is slightly better since the off-axis transmission of a coronagraph is a smooth function with the angular separation (Sivaramakrishnan et al. 2008). Here the contrast is defined as the coronagraphic PSF normalized by the peak of an off-axis source that is not affected by the FPM. This criterion accounts for the intensity reduction of an off-axis source due to the apodizer and Lyot stop. The average contrast is therefore calculated for each wavelength as follows using a numerical simulation:

$$\mathcal{C}_\lambda(\lambda) = \frac{1}{p}\frac{1}{(\mathcal{N}\lambda/\mathcal{D})^2}\int\int_{-(\mathcal{N}\lambda/2\mathcal{D})^2}^{(\mathcal{N}\lambda/2\mathcal{D})^2} |\Psi_D(\mathbf{r})|^2 d\mathbf{r} - \frac{1}{p}\frac{1}{(\mathcal{I}\lambda_0/\mathcal{D})^2|}\int_0^{\mathcal{I}\lambda_0/\mathcal{D}} |\Psi_D(r)|^2 2r dr, \tag{4}$$

where $\mathcal{D}$ is the telescope diameter, p is the maximum intensity of the off-axis PSF, $\mathcal{N}$ is the angular size of the dark zone as

described above, and $\mathcal{I}$ corresponds to a nominal geometric IWA defined by the angular diameter of the FPM at the central wavelength λ_0. Note that the dark zone size is a function of wavelength, but the IWA is set at the central wavelength to correspond to a unique physical angle on the sky. Finally, the criterion is averaged over the bandpass:

$$\mathcal{C} = \frac{1}{\Delta\lambda}\int_{\Delta\lambda} \mathcal{C}_\lambda(\lambda)d\lambda. \quad (5)$$

A different optimization criterion based on the Airy throughput (Vanderbei et al. 2003; Guyon et al. 2006) would be interesting to include the consideration of the useful flux of the planet, i.e., which fraction of the total planet flux can be used for detection. With an APLC, the off-axis PSF (planet) is simply the PSF produced by the apodized aperture, assuming that the source is sufficiently outside the focal plane mask area (outside the IWA). By definition for a prolate spheroidal apodization, this PSF has maximum encircled energy within a circle equal to the focal plane mask area. The fractional energy of the PSF within this circle is given by the eigenvalue Λ_0, which is very close to 1 for an APLC (typically $\Lambda_0 > 0.99$). This ensures that most of the planet flux is usable for detection with an APLC.

As shown in Section 2.2, the apodizer and mask size are given by the solution of a monochromatic eigenvalue problem, where the mask size corresponds to the eigenvalue and the apodizer to the eigenfunction. According to Equation (2), the mask size used for the eigenvalue calculation is set at the wavelength λ_1. In other words, the perfect APLC solution is only valid for the wavelength λ_1. The purpose of the broadband optimization is to select the best APLC solution to optimize the contrast over a finite bandpass motivated by science goals. Therefore, λ_1 is a free parameter in our optimization, in contrast to other studies where the APLC is defined at the longest wavelength of the band (Martinez et al. 2007). In order to have a clearly defined physical FPM size, we express the FPM angular diameter at the bandpass central wavelength λ_0, i.e., in units of $\lambda_0/\mathcal{D}$.

The parameters for the APLC optimization are as follows.

1. The telescope and mask geometry, which defines an eigenvalue problem with a set of generalized prolate spheroidal solutions. Here we consider circular focal plane masks.
2. The bandpass $\Delta\lambda$.
3. The FPM angular size at the central wavelength λ_0.
4. The wavelength λ_1 for which the eigenvalue and eigenfunctions are generated.
5. The Lyot stop outer diameter (OD) undersizing and inner diameter (ID) oversizing.

Because of the nonlinearity of the contrast criterion, special care is required to avoid possible local minima, and we explored a wide range of parameters to guide the optimization. In order to explore the parameter space for the criterion described by Equations (4) and (5), we generated a very large set of apodizations (eigenfunctions) for a fine grid of mask sizes (eigenvalues). We studied the convergence of the broadband contrast criterion with the number of wavelengths used in the simulation, and in practice we use a numerical integration of interpolated contrast values for a number of wavelengths across the band ($\simeq$20). This study is enabled by a fast propagation method (Soummer et al. 2007b) based on a semianalytical propagation combined with a matrix-based FT instead of the more commonly used fast Fourier transforms (FFTs). Using

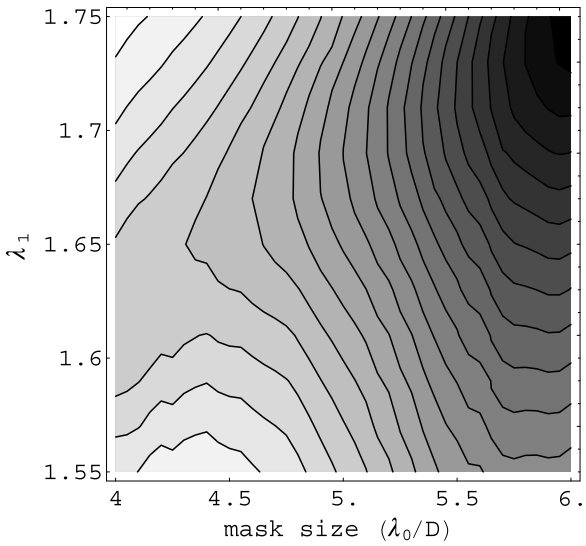

Figure 2. Average contrast criterion as a function of the angular mask diameter at the band center (x-axis) and as a function of the wavelength λ_1 (y-axis), which is used to calculate the apodizer. For the H band, the range of mask diameter varies from 0.17 to 0.26 arcsec (respectively $4\lambda_0/\mathcal{D}$ and $6\lambda_0/\mathcal{D}$). The Lyot stop geometry is fixed in this figure. This figure shows that there is no optimum for the mask diameter with this contrast criterion (the contours are equidistant in contrast). The average contrast in the dark zone continues to improve as the focal plane mask gets larger. Therefore, the FPM diameter is considered as a free parameter in the design. The contours show two regimes around $(4–5)\lambda/\mathcal{D}$ and $(5–6)\lambda/\mathcal{D}$. These two regimes correspond to the transition between "bell-shaped" and "bagel-shaped" apodizers, which depends on the particular telescope geometry. Note that one point in this figure corresponds to one APLC design, with one value of the average contrast criterion integrated over the bandpass. For example, for a mask size of $4.6\lambda_0/\mathcal{D}$, the optimal wavelength $\lambda_1 = 1.67\,\mu$m, and for $5.6\lambda_0/\mathcal{D}$, the optimal wavelength $\lambda_1 = 1.72\,\mu$m, with a contrast improvement by a factor of 23. The average contrast criterion as a function of wavelength is shown in Figure 4 for a few possible designs.

FFTs would lead to prohibitive computing time for our multidimensional parameter space study. The speed improvement is typically between one and two orders of magnitude, without any loss of numerical precision. Our preliminary optimization (Soummer 2005) did not involve as many search dimensions because of the limitations introduced by our use of FFTs.

In Figure 2, we show the evolution of the average contrast criterion for the H band (1.5–1.8 μm) and for the two main APLC parameters: the physical angular mask size defined at band center λ_0, and the wavelength λ_1 used to define the eigenvalue/eigenfunction set, and therefore the apodization function. Other parameters (Lyot stop geometry) play a weaker role in the optimization and are maintained constant in this figure. The parameter space is chosen for a range of mask diameters that are compatible with the science goals. For example, for the H band, $\lambda_0 = 1.65\,\mu$m. For an 8 m telescope, a mask diameter of $4\lambda_0/\mathcal{D}$ corresponds to 0.17 arcsec, and $6\lambda_0/\mathcal{D}$ to 0.26 arcsec. If for example the physical mask size is $5\lambda_0/\mathcal{D}$, and $\lambda_1 = 1.7\,\mu$m, the apodizer is calculated as the monochromatic solution at λ_1 for an angular mask size of 4.85 $\lambda_1/\mathcal{D}$.

For each mask size, there exists an optimum value for λ_1, which is larger than the band central wavelength λ_0 for mask sizes larger than $4.5\lambda_0/\mathcal{D}$. The larger the mask size, the larger the optimal wavelength λ_1. This is intuitively explained because a larger mask is always better than a smaller mask.

Using the average contrast criterion, we find that there is no unique optimum solution in terms of mask size and λ_1. The contrast keeps improving with larger mask sizes and larger

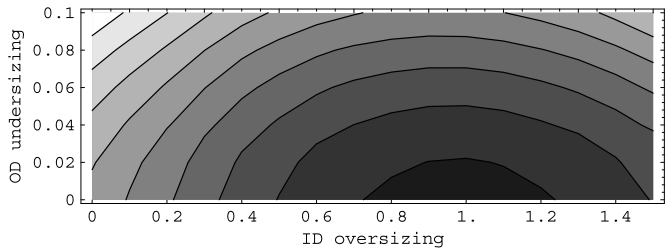

Figure 3. Average contrast criterion for the Lyot stop geometry as a function of inner diameter (ID) oversizing and outer diameter (OD) undersizing fractions. The mask diameter is $5.6\lambda_0/\mathcal{D}$, and $\lambda_1 = 1.72\,\mu$m. This shows that there is no optimum for the OD undersizing and in practice this value is set to match alignment tolerances (2% of the diameter). The ID shows an optimum value and typically the Lyot stops have a central obstruction doubled from the initial aperture geometry. For example, for an OD undersizing of 2%, the optimal ID oversizing is 98% for this particular solution. In this case, the contrast is improved by a factor of four compared to a 2% ID oversizing. See also Figure 10 for a qualitative explanation.

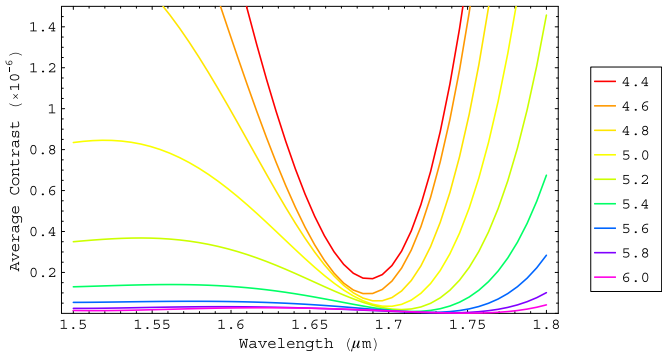

Figure 4. Average contrast in the dark zone as a function of wavelength across the H band, for a range of mask diameters from $4.4\lambda_0/\mathcal{D}$ to $6.0\lambda_0/\mathcal{D}$. The other parameters (wavelength λ_1 and Lyot stop geometry) are obtained using a numerical optimization. As the mask diameter increases the contrast improves at every wavelength and the chromaticity decreases as well. Quasi-achromatic solutions across most of the bandpass are obtained for mask diameters larger than $5.5\lambda_0/\mathcal{D}$.

(A color version of this figure is available in the online journal.)

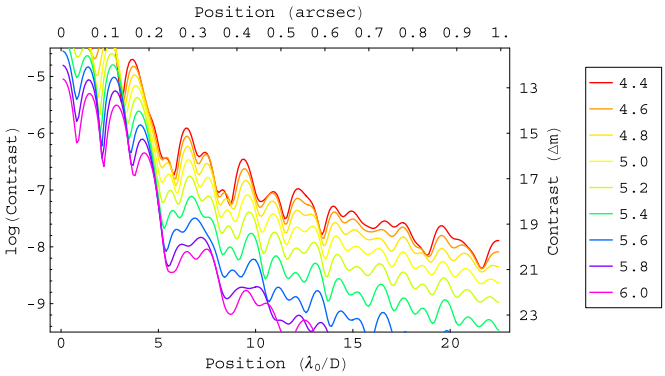

Figure 5. On-axis coronagraphic PSFs for the H band corresponding to the same parameters as in Figure 4. Again, this shows that the contrast improves monotonically with mask diameter. Because of the chromaticity improvement, the broadband contrast just outside the IWA can be improved dramatically with modest increase in mask diameter.

(A color version of this figure is available in the online journal.)

λ_1 values as well. In other words, the average contrast keeps improving with larger focal plane mask size. This result is independent of the Lyot stop geometry.

We show in Figure 3 the evolution of the average contrast criterion as a function of the Lyot stop geometry, specifically the ID oversizing fraction and the OD undersizing fraction. Here, we do not include the secondary mirror support structures, which are optimized independently. Undersizing the Lyot stop, OD does bring performance improvement. However, we set the OD undersizing fraction to 0.02 (2% of the diameter) to be compatible with alignment tolerances. The ID oversizing however shows a clear optimum, in this case around 100% oversizing, i.e., approximately doubling the size of the central obstruction in the Lyot plane.

Based on this parameter space study, there is no optimum for the mask diameter (Figure 2). We therefore select the physical mask size as an input parameter and then calculate the optimal wavelength λ_1 and the Lyot stop geometry (limited to the Lyot stop ID oversizing). The bandpass is a predefined constant, and the Lyot stop OD undersizing is set by optomechanical tolerances. The range of mask sizes we consider is roughly the one shown in Figure 2, and is constrained between a sufficient contrast performance and the need for a small IWA (0.2 arcsec IWA requirement for GPI). We use nonlinear optimization routines provided with the Mathematica software (Wolfram 2003) to search for the two optimization parameters. The choice of the mask size depends on the science requirements in terms of IWA (directly related to the mask radius) and contrast (contrast performance monotonically improves with mask size). In the next section, we discuss how increasing the mask size improves both contrast and achromaticity, and how we can select the appropriate mask size.

3.2. Quasi-achromatic Solutions for Gray Apodizers

3.2.1. Performance

In Figure 4, we show the average contrast $\mathcal{C}_\lambda(\lambda)$ as a function of wavelength, for FPM diameters ranging from 4.4 to 6.0 $\lambda_0/\mathcal{D}$. For each mask size, we use the nonlinear optimization to calculate the wavelength λ_1 and the Lyot stop geometry. This result confirms that the average contrast keeps improving as the mask diameter increases. For the Gemini telescope geometry and the H band, this set of calculations shows that smaller masks sizes below $5\lambda_0/\mathcal{D}$ lead to significant chromaticity, and that slightly larger mask sizes improve both the average contrast and the chromaticity performance, to reach a quasi-achromatic profile over most of the bandpass for masks sizes larger than $\simeq 5.5\lambda_0/\mathcal{D}$.

In Figure 5, we show the on-axis coronagraphic PSF for the H band and the same mask diameter as in Figure 4. This also illustrates how the contrast improves with increasing mask sizes. It is interesting to note that in this range, small increases in IWA can lead to very significant contrast improvement. For example, the contrast improves by about one order of magnitude just outside the IWA (5–$6\lambda_0/\mathcal{D}$), for a mask diameter increase between 5 and $5.6\lambda_0/\mathcal{D}$. Therefore, in this regime a modest increase of geometric IWA provides dramatic improvement of the coronagraphic PSF, which in turn helps the actual IWA since the perfect coronagraphic PSF contributes to residual pinned speckles.

In Soummer (2005), we used the encircled energy within the mask area in the final focal plane as the contrast criterion, using the semianalytical approach based on Hankel transform properties and numerical integration (Soummer et al. 2003a). The optimization approach was much simpler than the approach described here. The results presented here bring at least one order of magnitude improvement. The mask size used to calculate the apodization function was selected as a free parameter, for

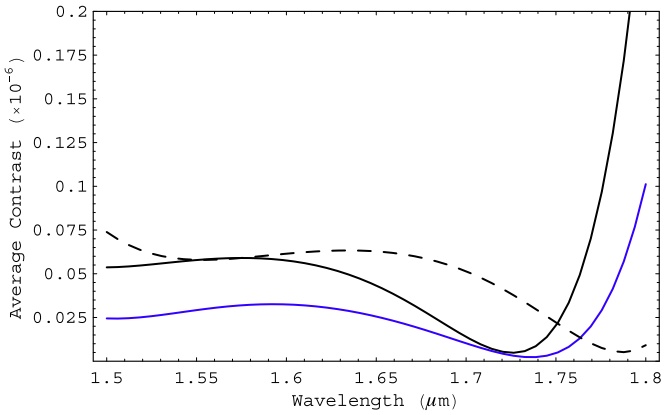

Figure 6. Black: average contrast for a $5.6\lambda_0/\mathcal{D}$ mask for the *H* band, where the two optimization parameters (λ_1 and ID) have been optimized using a nonlinear optimization routine. Because a change of mask size is formally equivalent to a change of wavelength, the long-wavelength degradation can be avoided by a translation of the curve to longer wavelengths, simply achieved using a larger mask size, e.g., $5.8\lambda_0/\mathcal{D}$ (black, dashed line). However, for this new larger mask size ($5.8\lambda_0/\mathcal{D}$), a re-optimization of the two parameters λ_1 and ID leads to a different apodizer and Lyot stop providing even better performance (blue line). (A color version of this figure is available in the online journal.)

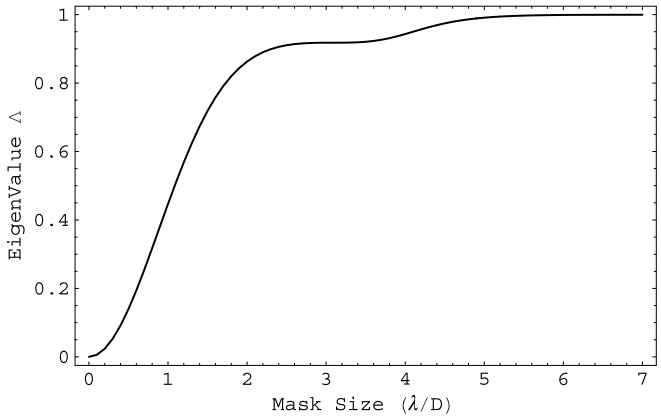

Figure 7. Eigenvalue Λ as a function of mask size for the generalized prolate spheroidal solution to a circular aperture with central obstruction corresponding the Gemini telescope geometry. Each eigenvalue corresponds to a different eigenfunction (the apodizer). In this case, the eigenvalue is calculated numerically. The eigenvalue is monotonic between 0 and 1. The inflection in the curve is due to the presence of the central obstruction and does not exist for a full aperture. Because a change of wavelength is formally equivalent to a change of mask size, the APLC becomes more achromatic as the mask size increases because of the saturation of the eigenvalue. The interesting quasi-achromatic regime for exoplanet detection is for a mask size $>5.5\lambda_0/\mathcal{D}$ in the flat region of the plot.

example $4\lambda/\mathcal{D}$. Then the physical focal plane mask was optimized for the entire band together with the other parameters (Lyot stop geometry). In this paper, the optimization is much more sophisticated because the solution of the eigenvalue problem (mask size and apodizer) is part of the optimization, i.e., a different apodization function (eigenfunction) is associated with each mask size (eigenvalue). For a given physical mask size, the apodization function changes with a change of the λ_1 value. These differences explain why the results presented here are a marked improvement over the earlier results of Soummer (2005).

In Figure 4, the monochromatic contrast criterion (Equation (4)) is always worse on the red side of the band. This is simply explained because for a given FPM, the PSF size scales with wavelength and therefore the mask is too large at shorter wavelengths and too small at longer wavelengths. Intuitively for a coronagraph, the performance degradation will be worse for a smaller mask than for a larger mask, and the contrast performance is mostly limited by the longest wavelength of the band. To first approximation, it is possible to use this property to optimize the APLC at the longest wavelength of the band, which typically gives better results than an optimization at band center. Martinez et al. (2007) compared these two approaches using a slightly different contrast criterion. However, their results show the existence of an optimum mask size, which we do not observe with our optimization scheme. This may be due to the slightly different criterion, or possibly to some other differences in the two optimization approaches. Their optimization includes the presence of several secondary mirror supports but do not include the Lyot stop optimization, while our approach includes the Lyot stop geometry, but not the secondary mirror supports. Their optimum mask size has slightly smaller values that what we typically use in this study, which may also explain the differences.

In Figure 6, one may wonder why we do not use a larger mask size to render the coronagraph even more achromatic. Since a change of mask size is formally equivalent to a change of wavelength, the contrast curve could be simply translated to longer wavelengths by using a larger mask. However, a complete optimization of the other parameters (including the apodization profile) for this larger mask size provides even better performance. Because we use an average contrast criterion over the bandpass, the performance always degrades on the red side of the band. A compromise could be found between average contrast and chromaticity by slightly modifying the criterion, for example by using a weighting function with wavelength. This could in principle provide an even more achromatic solution with slightly relaxed contrast performance.

3.2.2. Existence and Properties of Quasi-achromatic Solutions

The existence of quasi-achromatic solutions can be explained using a simple criterion using the properties of a prolate spheroidal function (Soummer et al. 2009a). An implicit relationship exists between the eigenvalue Λ_0 and the FPM diameter expressed in units of resolution elements ($\lambda_0/\mathcal{D}$), as shown in Figure 7 for an aperture geometry corresponding to the Gemini telescope. The inflection in the curve is due to the presence of central obstruction (this feature does not exist in the eigenvalue for a full circular aperture; Soummer et al. 2003a). As discussed in Section 2.2, a change of wavelength is formally equivalent to a change of mask diameter, and therefore also formally equivalent to a change of eigenvalue. As shown in Figure 1, the achromatic APLC solution is obtained by adjusting the apodization function with wavelength to the corresponding eigenvalue (Aime 2005). For large mask diameters, the eigenvalue curve saturates and therefore the eigenvalue is relatively insensitive to a change of mask size (or wavelength). Therefore, the corresponding eigenfunction is also relatively insensitive to the mask size (or wavelength). As a result, the chromaticity of the APLC becomes negligible for large masks in the region where the eigenvalue saturates. In other words, a gray apodizer naturally approximates the achromatic solution of Aime (2005) for large mask diameters. Fortunately, the regime where these quasi-achromatic solutions appear is situated in a region of "reasonable" mask diameters ($\simeq 5.5\lambda_0/\mathcal{D}$ in diameter) in the case of the Gemini telescope geometry. However, this region is a function of both bandpass and aperture geometry and the result may vary for other telescopes and bandpasses of interest. This property is particularly attractive for ELTs, which have very high

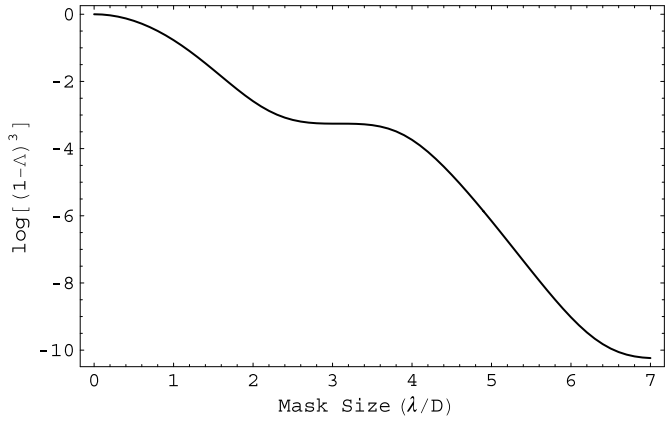

Figure 8. Residual energy can be obtained directly from the eigenvalue Λ as $(1-\Lambda)^2$ (Aime et al. 2002; Soummer et al. 2003a). For slightly larger mask size, the APLC can have a much higher monochromatic rejection and the chromaticity decreases as well. The inflection in the curve around $3\lambda_0/\mathcal{D}$ is due to the presence of the central obstruction and does not exist for a full aperture. The quasi-achromatic region is found in the linear region of this plot ($>5.5\lambda_0/\mathcal{D}$), where the residual energy decreases exponentially. The derivative of the residual energy is related to the chromaticity and is also decreasing exponentially in this region.

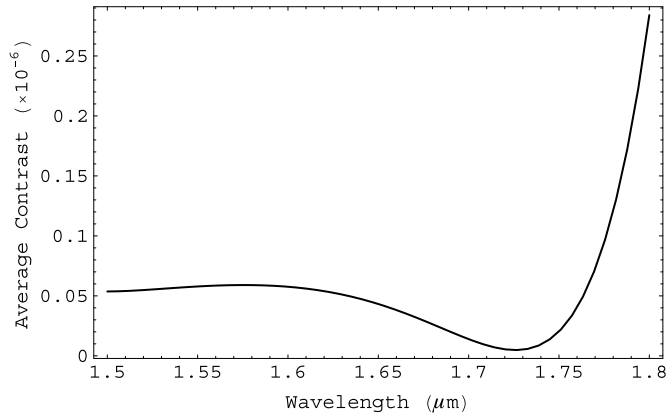

Figure 9. Average contrast in the dark zone outside the IWA for the case of GPI. The mask diameter is $5.6\lambda_0/\mathcal{D}$ at band center, which corresponds to $\simeq$0.24 arcsec in diameter.

angular resolution, and can afford to trade a slightly larger mask for improved performance (Martinez et al. 2008; Soummer et al. 2009a).

Following the notations of Soummer et al. (2009a), the total energy in the final image outside an area equivalent to the FPM finds a simple expression as a function of the eigenvalue Λ_0:

$$e_{om} = (1-\Lambda_0)^3. \quad (6)$$

We show this residual energy in logarithmic scale in Figure 8. Between $5\lambda_0/\mathcal{D}$ and $6\lambda_0/\mathcal{D}$, the rejection decreases approximately exponentially, which confirms that in this region a modest increase in mask diameter leads to significant contrast improvement, and that the chromaticity is dramatically reduced as well. The chromaticity is related to the derivative of the residual energy with wavelength (or mask size). In this region, the chromaticity decreases qualitatively exponentially.

3.2.3. Application to the Gemini Planet Imager

Figure 9 shows the average contrast for the GPI design, which has a mask diameter of $5.6\lambda_0/\mathcal{D}$. The corresponding broadband intensities in the Lyot plane are shown in Figure 10. The design

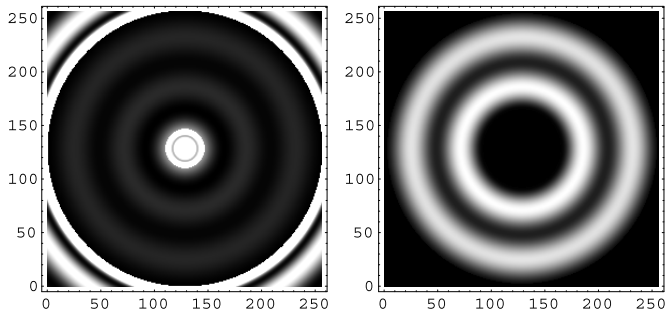

Figure 10. Left: broadband image of the Lyot plane before application of the Lyot stop. Note the sharp and bright outer edge of the aperture, which illustrates why undersizing the Lyot stop does not improve contrast performance in this case. Right: broadband image after application of the Lyot stop. The significantly oversized central obstruction is about twice the original size. Note that the optimization selected the central obstruction inner diameter so that the intensity profile in the Lyot plane is also apodized along the central obstruction. Any other Lyot stop inner diameter would create a sharp discontinuity that would diffract more light in the focal plane and therefore degrade the contrast performance.

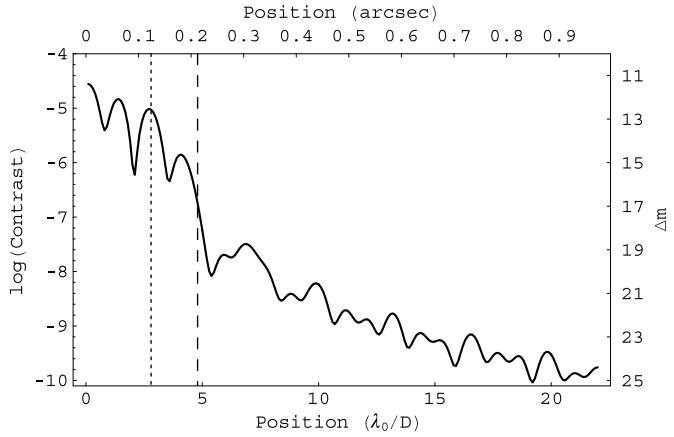

Figure 11. On-axis coronagraphic PSF for the GPI design in the absence of aberrations, averaged for the H band. The average broadband contrast is better than 10^{-7} for separations larger than $\simeq 5\lambda_0/\mathcal{D}$ ($\simeq$ 0.2 arcsec).

is optimized for the telescope geometry, with a telescope OD of 7.770 m and ID 1.023 m. The aperture is slightly undersized to account for 2% lateral alignment tolerances. The broadband coronagraphic PSF for the H band is shown in Figure 11. This design satisfies the requirement of 10^{-7} contrast at 0.2 arcsec (Macintosh et al. 2008).

4. CONCLUSION

In this paper, we detailed the chromatic properties of APLCs and studied the numerical optimization of these coronagraphs in broadband assuming a gray apodizer. We find that both the average contrast and the chromatic performance improve monotonically with the mask diameter, and we find a quasi-achromatic regime for masks larger than $\simeq 5.5\lambda_0/\mathcal{D}$ for the geometry of the Gemini telescope and the H band. The existence of the quasi-achromatic behavior is discussed in light of the mathematical properties of generalized prolate spheroidal functions used to define the apodization for on-axis telescopes. We explored the parameter space to determine which parameters need to be optimized, and we illustrate the results with the design of the coronagraph for the GPI. The high achromaticity of this design translates into very good simultaneous spectral differential imaging performance (Marois et al. 2008b). This

coronagraph has been built in the laboratory (Soummer et al. 2009b; Sivaramakrishnan et al. 2009; Sivaramakrishnan et al. 2010) according to this design, and will be integrated in the GPI instrument in 2010, for science operations starting in 2011. This approach was also used to optimize the Palomar project 1640 coronagraph used at the Hale telescope (Hinkley et al. 2010a, 2010b; Zimmerman et al. 2010), which operates in conjunction with an integral field spectrograph over the J and H bands (1.05–1.75 μm).

Portions of this work were performed under the auspices of the U.S. Department of Energy by the Lawrence Livermore National Laboratory under Contract DE-AC52-07NA27344. The authors would like to thank the Gemini Planet Imager team for assistance with development of the GPI coronagraph design and technical information about the instrument, and the Association of Universities for Research in Astronomy for supporting the construction of the Gemini Planet Imager. R.S. acknowledges support from the American Museum of Natural History Kalbfleisch Fellowship. L.P.'s work was performed in part under contract with the California Institute of Technology (Caltech) funded by NASA through the Sagan Fellowship Program and in part by an appointment to the NASA Postdoctoral Program at the Jet Propulsion Laboratory, Caltech, administered by Oak Ridge Associated Universities through a contract with NASA. Project 1640 is funded by National Science Foundation grants AST-0520822, AST-0804417, and AST-0908484. This work was also supported in part by the NSF Science and Technology CfAO, managed by the UC Santa Cruz under cooperative agreement AST 98-76783. The authors would like to thank the Gemini Planet Imager team for assistance with development of the GPI coronagraph design and technical information about the instrument and in particular Christian Marois and James Graham for discussions, and also thank Claude Aime and Andrea Ferrari for discussions on APLCs.

REFERENCES

Aime, C. 2005, PASP, 117, 1012
Aime, C., & Soummer, R. 2004, ApJ, 612, L85
Aime, C., Soummer, R., & Ferrari, A. 2002, A&A, 389, 334
Baraffe, I., Chabrier, G., Barman, T. S., Allard, F., & Hauschildt, P. H. 2003, A&A, 402, 701
Baudoz, P., Rabbia, Y., & Gay, J. 2000, A&A, 141, 319
Beuzit, J.-L., et al. 2008, Proc. SPIE, 7014, 701418
Bloemhof, E. E. 2003, ApJ, 582, L59
Bloemhof, E. E., Dekany, R. G., Troy, M., & Oppenheimer, B. R. 2001, ApJ, 558, L71
Burrows, A., Sudarsky, D., & Hubeny, I. 2004, ApJ, 609, 407
Cady, E., Macintosh, B., Kasdin, N. J., & Soummer, R. 2009, ApJ, 698, 938
Carlotti, A., Ricort, G., Aime, C., El Azhari, Y., & Soummer, R. 2008, A&A, 477, 329
Crepp, J. R., et al. 2011, ApJ, 729, 132
Fitzgerald, M. P., & Graham, J. R. 2006, ApJ, 637, 541
Foo, G., Palacios, D. M., & Swartzlander, G. A., Jr. 2005, Opt. Lett., 30, 3308
Guyon, O., Pluzhnik, E. A., Galicher, R., Martinache, F., Ridgway, S. T., & Woodruff, R. A. 2005, ApJ, 622, 744
Guyon, O., Pluzhnik, E. A., Kuchner, M. J., Collins, B., & Ridgway, S. T. 2006, ApJS, 167, 81
Hinkley, S., Oppenheimer, B. R., Brenner, D., Parry, I. R., Sivaramakrishnan, A., Soummer, R., & King, D. 2008, Proc. SPIE, 7015, 701519
Hinkley, S., et al. 2010, ApJ, 712, 421
Hinkley, S., et al. 2011, PASP, in press (arXiv:1012.0008)
Hodapp, K. W., et al. 2008, Proc. SPIE, 7014, 701419
Janson, M., Bergfors, C., Goto, M., Brandner, W., & Lafrenière, D. 2010, ApJ, 710, L35
Kalas, P., et al. 2008, Science, 322, 1345
Kasdin, N. J., Vanderbei, R. J., Spergel, D. N., & Littman, M. G. 2003, ApJ, 582, 1147
Krist, J. E., Shaklan, S. B., & Levine, M. B. 2008, Proc. SPIE, 7010, 701044
Kuchner, M. J., & Traub, W. A. 2002, ApJ, 570, 900
Lafrenière, D., Marois, C., Doyon, R., Nadeau, D., & Artigau, É. 2007, ApJ, 660, 770
Lagrange, A.-M., et al. 2009, A&A, 493, L21
Lyot, B. 1939, MNRAS, 99, 538
Macintosh, B. A., et al. 2008, Proc. SPIE, 7015, 701518
Marley, M. S., Fortney, J. J., Hubickyj, O., Bodenheimer, P., & Lissauer, J. J. 2007, ApJ, 655, 541
Marois, C., Doyon, R., Racine, R., & Nadeau, D. 2000, PASP, 112, 91
Marois, C., Lafrenière, D., Doyon, R., Macintosh, B., & Nadeau, D. 2006, ApJ, 641, 556
Marois, C., Macintosh, B., Barman, T., Zuckerman, B., Song, I., Patience, J., Lafrenière, D., & Doyon, R. 2008a, Science, 322, 1348
Marois, C., Macintosh, B., Soummer, R., Poyneer, L., & Bauman, B. 2008b, Proc. SPIE, 7015, 70151
Martinache, F., & Guyon, O. 2009, Proc. SPIE, 7440, 74400
Martinache, F., Guyon, O., Pluzhnik, E. A., Galicher, R., & Ridgway, S. T. 2006, ApJ, 639, 1129
Martinez, P., Boccaletti, A., Kasper, M., Baudoz, P., & Cavarroc, C. 2007, A&A, 474, 671
Martinez, P., Boccaletti, A., Kasper, M., Cavarroc, C., Yaitskova, N., Fusco, T., & Vérinaud, C. 2008, A&A, 492, 289
Martinez, P., Dorrer, C., Aller Carpentier, E., Kasper, M., Boccaletti, A., Dohlen, K., & Yaitskova, N. 2009, A&A, 495, 363
Martinez, P., Dorrer, C., Kasper, M., Boccaletti, A., & Dohlen, K. 2009, A&A, 500, 1281
Mawet, D., Riaud, P., Absil, O., & Surdej, J. 2005, ApJ, 633, 1191
Oppenheimer, B. R., & Hinkley, S. 2009, ARA&A, 47, 253
Oppenheimer, B. R., et al. 2004, Proc. SPIE, 5490, 433
Perrin, M. D., Sivaramakrishnan, A., Makidon, R., Oppenheimer, B. R., & Graham, J. R. 2003, ApJ, 596, 702
Pluzhnik, E. A., Guyon, O., Ridgway, S. T., Martinache, F., Woodruff, R. A., Blain, C., & Galicher, R. 2006, ApJ, 644, 1246
Roddier, F., & Roddier, C. 1997, PASP, 109, 815
Rouan, D., Riaud, P., Boccaletti, A., Clénet, Y., & Labeyrie, A. 2000, PASP, 112, 1479
Schneider, J. 2010, Extrasolar Planets Encyclopaedia,http://exoplanet.eu/
Serabyn, E., Mawet, D., & Burruss, R. 2010, Nature, 464, 1018
Sivaramakrishnan, A., Koresko, C. D., Makidon, R. B., Berkefeld, T., & Kuchner, M. J. 2001, ApJ, 552, 397
Sivaramakrishnan, A., & Lloyd, J. P. 2005, ApJ, 633, 528
Sivaramakrishnan, A., Lloyd, J. P., Hodge, P. E., & Macintosh, B. A. 2002, ApJ, 581, L59
Sivaramakrishnan, A., Soummer, R., Carr, G. L., Dorrer, C., Bolognesi, A., Zimmerman, N., & Oppenheimer, B. R. 2009, Proc. SPIE, 7440, 74401
Sivaramakrishnan, A., Soummer, R., Pueyo, L., Wallace, J. K., & Shao, M. 2008, ApJ, 688, 701
Sivaramakrishnan, A., et al. 2010, Proc. SPIE, 7735, 773586
Slepian, D. 1964, Bell Syst. Tech. J., 43, 3009
Soummer, R. 2005, ApJ, 618, L161
Soummer, R., Aime, C., & Falloon, P. E. 2003a, A&A, 397, 1161
Soummer, R., Aime, C., Ferrari, A., Sivaramakrishnan, A., Oppenheimer, B. R., Makidon, R., & Macintosh, B. 2006, in IAU Colloq. 200, Direct Imaging of Exoplanets: Science and Techniques, ed. C. Aime & F. Vakili (Cambridge: Cambridge Univ. Press), 367
Soummer, R., Dohlen, K., & Aime, C. 2003b, A&A, 403, 369
Soummer, R., Ferrari, A., Aime, C., & Jolissaint, L. 2007a, ApJ, 669, 642
Soummer, R., Pueyo, L., Ferrari, A., Aime, C., Sivaramakrishnan, A., & Yaitskova, N. 2009a, ApJ, 695, 695
Soummer, R., Pueyo, L., Sivaramakrishnan, A., & Vanderbei, R. J. 2007b, Opt. Express, 15, 15935
Soummer, R., et al. 2009b, Proc. SPIE, 7440, 74400
Sparks, W. B., & Ford, H. C. 2002, ApJ, 578, 543
Vanderbei, R. J., Spergel, D. N., & Kasdin, N. J. 2003, ApJ, 599, 686
Wallace, J. K., et al. 2008, Proc. SPIE, 7015, 70156
Wolfram, S. 2003, The Mathematica Book (5th ed.; Oxford: Wolfram Media, Inc.)
Zimmerman, N., et al. 2010, ApJ, 709, 733